INTERNATIONAL JOURNAL FOR NUMERICAL METHODS IN FLUIDS, VOL. 23, 347–366 (1996)

FLUX DIFFERENCE SPLITTING FOR THREE-DIMENSIONAL STEADY INCOMPRESSIBLE NAVIER–STOKES EQUATIONS IN CURVILINEAR CO-ORDINATES

C. W. OOSTERLEE AND H. RITZDORF

German National Research Center for Information Technology, Institute for Algorithms and Scientific Computing (GMD, SCAI),
Schloss Birlinghoven, D-53754 St. Augustin, Germany

SUMMARY

A collocated discretization of the 3D steady incompressible Navier–Stokes equations based on a flux-difference-splitting formulation is presented. The discretization employs primitive variables of Cartesian velocity components and pressure. The splitting used here is a polynomial splitting introduced by Dick and Linden of Roe type. Second-order accuracy is obtained with the defect correction approach in which the state vector is interpolated with van Leer's κ-scheme. The underlying solution technique to solve the discretized equations is a parallel multiblock multigrid method. Several 2D and 3D test problems such as driven cavity and channel flows are solved.

KEY WORDS three-dimensional incompressible Navier–Stokes; collocated grid; curvilinear co-ordinates; flux difference splitting; defect correction; multigrid

1. INTRODUCTION

For the discretization and solution of the steady incompressible Navier–Stokes equations in arbitrarily shaped domains, several methods have been proposed. With the finite element method, very complex geometries can be discretized. However, for solving finite element dicretizations, it is a disadvantage that the sparsity pattern of a discretized operator is not regular. Therefore it can be difficult to find robust solution methods. A compromise between flexibility and robustness is the use of finite volume discretizations on block-structured grids. In a general domain, then, a boundary-fitted curvilinear grid is generated. With multiblock methods the flexibility of these finite volume methods is increased. The regular sparsity pattern in these discretizations can be employed for robustness and efficiency aspects of solution methods. The discretization methods adopting boundary-fitted curvilinear co-ordinate systems differ in grid arrangement (collocated or staggered grids) and in the choice of velocity components (Cartesian or so-called grid-oriented velocity unknowns such as contravariant components). Nowadays, discretization techniques that have proved to be successful and promising for 2D problems are being generalized to three dimensions. An (incomplete) overview of some of these techniques is given now.

The first approach where complex flows are solved successfully employs a combination of *staggered grids* and *contravariant flux* unknowns and pressure as dependent variables. It is for example used in References 1 and 2, where also 3D problems were tackled. The same combination was used in a different fashion in Reference 3, for which 3D flow was shown in Reference 4. Another recent paper

CCC 0271–2091/96/040347–20

Received 5 December 1994
Revised 1 November 1995

with 3D equations solved on a staggered grid, and where the appearance of Christoffel symbols is avoided, is Reference 5. In Japan, staggered grids are widely investigated, for example in Reference 6 for 2D and in Reference 7 for 3D problems with dependent variables of contravariant fluxes V^α and contravariant vorticities.

The second and probably the most widely adopted approach to discretizing the incompressible Navier–Stokes equations in curvilinear co-ordinates is to use *Cartesian* velocity unknowns and pressure as dependent variables on a *collocated* grid. The pioneering paper of this collocated approach is by Rhie and Chou.[8] A lot of research on discretizations for non-staggered grids with Cartesian velocity unknowns is also presented in References 9 and 10, where a set of benchmark solutions is proposed for the 2D incompressible Navier–Stokes equations in non-orthogonal domains. This approach is generalized to three dimensions in many papers: in References 11 and 12, where steady and unsteady, 2D and 3D problems are solved, and in Reference 13, where the unsteady incompressible Navier–Stokes and Boussinesq equations are tackled. For efficient solution of the steady equations, sometimes pseudocompressibility methods are adopted. With an artificial time-dependent pressure term in the continuity equation the incompressible Navier–Stokes equations can be approached with methods from the compressible Navier–Stokes equations. This method is for example presented for a 3D collocated discretization in curvilinear co-ordinates in References 14 and 15, where also an advanced upwind scheme based on flux difference splitting is incorporated.

In this paper the collocated approach is also adopted. The discretization which is generalized to three dimensions here is presented in Reference 16. With a flux-splitting formulation of the steady incompressible Navier–Stokes equations, well-known discretization and solution methods coming from the steady compressible Navier–Stokes equations,[17,18] but not based on pseudocompressibility methods, can be used. Solution methods for the steady equations reach small residuals or order 10^{-6} much faster than time-accurate methods.

It is hard to say which approach is best in general co-ordinates. With pseudocompressibility methods it is difficult to achieve accurate mass conservation, especially for time-dependent flows. The other non-staggered methods require stabilization measures that may influence accuracy and may require tuning. In our discretization method the stabilization comes in naturally with flux splitting. The 3D incompressible Navier–Stokes equations are discretized on a block-structured grid with vertex-centred finite volumes. A first-order-accurate upwind discretization with polynomial flux difference splitting[16] is used. With defect correction, second-order accuracy is obtained with van Leer's second-order κ-scheme.[19] Parallel multigrid is used to solve the steady equations directly as inner iteration in the defect correction technique.[17,20,21]

At GMD a 2D incompressible Navier–Stokes code has been developed as part of the L_iSS package.[22] L_iSS is a programme package for solving partial differential equations on general domains. The parallel solution of equations has been focused upon by constructing parallel multigrid solution methods and parallelization tools such as a communications library based on PARMACS.[23] The parallelization strategy adopted is the grid-partitioning method (explained in Reference 24).

In this paper we merely concentrate on the accuracy of the flow results obtained and on multigrid convergence results. A detailed comparison of the multiblock multigrid convergence for 2D and 3D problems as well as CPU time results is the subject of a forthcoming paper.

Here several results will be presented, for example two benchmark problems that were proposed in Reference 10 for discretizations on non-orthogonal grids in two dimensions. Also 3D equivalents will be solved as well as 3D channel flows.

2. FLUX DIFFERENCE SPLITTING FOR INCOMPRESSIBLE NAVIER–STOKES EQUATIONS

In Cartesian co-ordinates the steady incompressible Navier–Stokes equations are given by

$$
\begin{aligned}
&\frac{\partial u^2}{\partial x}+\frac{\partial uv}{\partial y}+\frac{\partial uw}{\partial z}+\frac{\partial p}{\partial x}=\frac{1}{Re}\left(\frac{\partial^2 u}{\partial x^2}+\frac{\partial^2 u}{\partial y^2}+\frac{\partial^2 u}{\partial z_2}\right),\\
&\frac{\partial uv}{\partial x}+\frac{\partial v^2}{\partial y}+\frac{\partial vw}{\partial z}+\frac{\partial p}{\partial y}=\frac{1}{Re}\left(\frac{\partial^2 v}{\partial x^2}+\frac{\partial^2 v}{\partial y^2}+\frac{\partial^2 v}{\partial z^2}\right),\\
&\frac{\partial uw}{\partial x}+\frac{\partial vw}{\partial y}+\frac{\partial w^2}{\partial z}+\frac{\partial p}{\partial z}=\frac{1}{Re}\left(\frac{\partial^2 w}{\partial x^2}+\frac{\partial^2 w}{\partial y^2}+\frac{\partial^2 w}{\partial z^2}\right),\\
&c^2\left(\frac{\partial u}{\partial x}+\frac{\partial v}{\partial y}+\frac{\partial w}{\partial z}\right)=0.
\end{aligned}
\tag{1}
$$

Here u, v, and w are the Cartesian velocity unknowns, p is the pressure, c is a constant reference velocity and Re is the Reynolds number defined as

$$Re=\bar{U}L/\nu, \tag{2}$$

where $\bar{U}$ is a characteristic velocity, L is a characteristic length and ν is the kinematic viscosity.

The system of equations (1) is written in conservative form as

$$\frac{\partial \mathbf{f}}{\partial x}+\frac{\partial \mathbf{g}}{\partial y}+\frac{\partial \mathbf{h}}{\partial z}=\frac{\partial \mathbf{f}_\mathrm{v}}{\partial x}+\frac{\partial \mathbf{g}_\mathrm{v}}{\partial y}+\frac{\partial \mathbf{h}_\mathrm{v}}{\partial z}, \tag{3}$$

where **f**, **g** and **h** are the components of the convective flux vector given by

$$
\mathbf{f}=\begin{bmatrix}u^2+p\\ uv\\ uw\\ c^2u\end{bmatrix},\qquad
\mathbf{g}=\begin{bmatrix}uv\\ v^2+p\\ vw\\ c^2v\end{bmatrix},\qquad
\mathbf{h}=\begin{bmatrix}uw\\ vw\\ w^2+p\\ c^2w\end{bmatrix}
$$

and $\mathbf{f}_\mathrm{v}$, $\mathbf{g}_\mathrm{v}$ and $\mathbf{h}_\mathrm{v}$ are the viscous fluxes given by

$$
\mathbf{f}_\mathrm{v}=\begin{bmatrix}(1/Re)\partial u/\partial x\\ (1/Re)\partial v/\partial x\\ (1/Re)\partial w/\partial x\\ 0\end{bmatrix},\qquad
\mathbf{g}_\mathrm{v}=\begin{bmatrix}(1/Re)\partial u/\partial y\\ (1/Re)\partial v/\partial y\\ (1/Re)\partial w/\partial y\\ 0\end{bmatrix},\qquad
\mathbf{h}_\mathrm{v}=\begin{bmatrix}(1/Re)\partial u/\partial z\\ (1/Re)\partial v/\partial z\\ (1/Re)\partial w/\partial z\\ 0\end{bmatrix}.
$$

Differences with respect to **u** of the convective fluxes can be written as

$$\Delta\mathbf{f}=A_1\Delta\mathbf{u},\qquad \Delta\mathbf{g}=A_2\Delta\mathbf{u},\qquad \Delta\mathbf{h}=A_3\Delta\mathbf{u}. \tag{4}$$

Here $\mathbf{u}=(u,v,w,p)^\mathrm{T}$ and A_1, A_2 and A_3 are the discrete Jacobians given by

$$
A_1=\begin{bmatrix}2\bar{u}&0&0&1\\ \bar{v}&\bar{u}&0&0\\ \bar{w}&0&\bar{u}&0\\ c^2&0&0&0\end{bmatrix},\qquad
A_2=\begin{bmatrix}\bar{v}&\bar{u}&0&0\\ 0&2\bar{v}&0&1\\ 0&\bar{w}&\bar{v}&0\\ 0&c^2&0&0\end{bmatrix},\qquad
A_3=\begin{bmatrix}\bar{w}&0&\bar{u}&0\\ 0&\bar{w}&\bar{v}&0\\ 0&0&2\bar{w}&1\\ 0&0&c^2&0\end{bmatrix},
$$

where the overbar denotes the mean of variables.

The matrix A will be written as a combination of A_1, A_2 and A_3:

$$A = n_xA_1 + n_yA_2 + n_zA_3 = \begin{bmatrix} n_x\bar{u} + r & n_y\bar{u} & n_z\bar{u} & n_x \\ n_x\bar{v} & n_y\bar{v} + r & n_z\bar{v} & n_y \\ n_x\bar{w} & n_y\bar{w} & n_z\bar{w} + r & n_z \\ n_xc^2 & n_yc^2 & n_zc^2 & 0 \end{bmatrix}, \tag{5}$$

where $r = n_x\bar{u} + n_y\bar{v} + n_z\bar{w}$ and n_x, n_y and n_z are the components of a normal vector. Using $n_x^2 + n_y^2 + n_z^2 = 1$, a set of three different eigenvectors is found for the matrix A:

$$\lambda_1 = \lambda_2 = r, \qquad \lambda_3 = r + a, \qquad \lambda_4 = r - a, \tag{6}$$

with $a = \sqrt{}(r^2 + c^2)$.

However, a full set of four left and right eigenvectors was found. This is done semi-automatically with the help of the symbolic manipulation programme REDUCE.[25] The matrix A will be split into negative and positive parts A^- and A^+:

$$A = A^- + A^+, \qquad A^- = R\Lambda^-L, \qquad A^+ = R\Lambda^+L, \tag{7}$$

where

$$\Lambda^- = \begin{bmatrix} \lambda_1^- & 0 & 0 & 0 \\ 0 & \lambda_2^- & 0 & 0 \\ 0 & 0 & \lambda_3^- & 0 \\ 0 & 0 & 0 & \lambda_4^- \end{bmatrix}, \quad \Lambda^+ = \begin{bmatrix} \lambda_1^+ & 0 & 0 & 0 \\ 0 & \lambda_2^+ & 0 & 0 \\ 0 & 0 & \lambda_3^+ & 0 \\ 0 & 0 & 0 & \lambda_4^+ \end{bmatrix}, \quad \lambda_i^+ = \max(\lambda_i, 0), \quad \lambda_i^- = \min(\lambda_i, 0).$$

Now, using (5) and (7), a linear combination of flux differences can be expressed as

$$n_x\Delta\mathbf{f} + n_y\Delta\mathbf{g} + n_z\Delta\mathbf{h} = (A^- + A^+)\Delta\mathbf{u}. \tag{8}$$

3. FINITE VOLUME DISCRETIZATION

This section is a three-dimensional continuation of the two-dimensional discretization in Reference 16. The formula chosen to calculate a 3D volume is found in Reference 26 (p.17) and is also used in Reference 1. Each volume is computed by dividing it into three pyramids having the main diagonal and one vertex of the volume in common; see Figure 1. In the formula in Figure 1, $s_{i,j,k,l}$ denotes the face through i, j, k and l and $\mathbf{r}_{i,j}$ denotes the vector between i and j. The volume is found with inner products between $\mathbf{s}_{i,j,k,l}$ and $\mathbf{r}_{i,j}$.

Finite volume integration of the inviscid part of (3) over the control volume $\Omega_{i,j,k}$ gives

$$\int_{\Omega_{i,j,k}} \left(\frac{\partial\mathbf{f}}{\partial x} + \frac{\partial\mathbf{g}}{\partial y} + \frac{\partial\mathbf{h}}{\partial z}\right)\partial\Omega = F_{i+1/2,j,k} + F_{i-1/2,j,k} + F_{i,j+1/2,k} + F_{i,j-1/2,k} + F_{i,j,k+1/2} + F_{i,j,k-1/2}. \tag{9}$$

To evaluate the term $F_{i+1/2,j,k}$ in (9), $F_{i,j,k}$ is defined as an approximation from the grid point (i, j, k):

$$F_{i,j,k} = \mathrm{d}S_{i+1/2,j,k}(n_x\mathbf{f} + n_y\mathbf{g} + n_z\mathbf{h})|_{i,j,k}, \tag{10}$$

where $\mathbf{f}, \mathbf{g}, \mathbf{h}|_{i,j,k}$ denote that $\mathbf{u}$-values from $(i, j, k)^{\mathrm{T}}$ are used, $(n_x, n_y, n_z)^{\mathrm{T}}$ is the outward normal vector on the volume side and $\mathrm{d}S$ is the length of the volume side. $F_{i+1,j,k}$ is defined similarly as an approximation from $(i + 1, j, k)$:

$$F_{i+1,j,k} = \mathrm{d}S_{i+1/2,j,k}(n_x\mathbf{f} + n_y\mathbf{g} + n_z\mathbf{h})|_{i+1,j,k}. \tag{11}$$

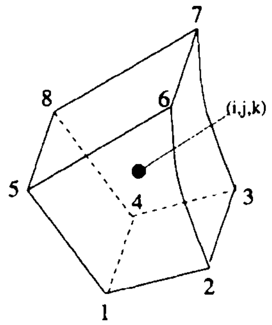

Figure 1. The formula to calculate the volume: $\Omega_{i,j,k} = \frac{1}{3}\{(\mathbf{s}_{5,8,7,6} + \mathbf{s}_{3,7,8,4}).(\mathbf{r}_{8,7} - \mathbf{r}_{1,4}) + (\mathbf{s}_{1,5,6,2} + \mathbf{s}_{2,6,7,3}.(\mathbf{r}_{2,6} - \mathbf{r}_{1,4})\}$

For the flux $F_{i+1/2,j,k}$ an upwind definition is used:

$$F_{i+1/2,j,k} = \tfrac{1}{2}(F_{i,j,k} + F_{i+1,j,k} - |\Delta F_{i,i+1}|), \tag{12}$$

where, as explained in Reference 16, $\Delta F_{i,i+1}$ is defined as

$$\Delta F_{i,i+1} = F_{i+1,j,k} - F_{i,j,k} = \mathrm{d}S_{i+1/2,j,k} A_{i,i+1} \Delta \mathbf{u}_{i,i+1}. \tag{13}$$

Here $A_{i,i+1}$ is built as in (5), with $\bar{\mathbf{u}}$-values coming from $(i, j, k)^{\mathrm{T}}$ and $(i+1, j, k)^{\mathrm{T}}$, and $\Delta \mathbf{u}_{i,i+1} = \mathbf{u}_{i+1,j,k} - \mathbf{u}_{i,j,k}$. With (7) it now follows that for the absolute value of $\Delta F_{i,i+1}$ is found

$$|\Delta F_{i,i+1}| = \mathrm{d}S_{i+1/2,j,k}(A^{+}_{i,i+1} - A^{-}_{i,i+1})\Delta \mathbf{u}_{i,i+1}. \tag{14}$$

The formula used in the discretization is found with (8), (10), (12) and (13):

$$\begin{aligned} F_{i+1/2,j,k} &= F_{i,j,k} + \tfrac{1}{2}(F_{i+1,j,k} - F_{i,j,k}) - \tfrac{1}{2}|\Delta F_{i,i+1}| \\ &= F_{i,j,k} + \tfrac{1}{2}\mathrm{d}S_{i+1/2,j,k}(n_x \mathbf{f} + n_y \mathbf{g} + n_z \mathbf{h})|_{i,i,+1} - \tfrac{1}{2}|\Delta F_{i,i+1}| \\ &= F_{i,j,k} + \mathrm{d}S_{i+1/2,j,k} A^{-}_{i,i+1} \Delta \mathbf{u}_{i,i+1}. \end{aligned} \tag{15}$$

The fluxes on the other volume boundaries in (9) are treated in the same way.

The viscous fluxes $\mathbf{f}_{\mathrm{v}}$, $\mathbf{g}_{\mathrm{v}}$ and $\mathbf{h}_{\mathrm{v}}$ are discretized with the Peyret control volume technique.[27] The second derivatives disappear with a shifted control volume.[16,27]

Also the treatment of boundary conditions which is described in detail in Reference 16 is generalized to three dimensions. For solid wall Dirichlet conditions the velocity is prescribed, while the pressure at boundary points is found with an equation for the pressure coming from the continuity equation corrected with contributions from the momentum equations. At outflow, Neumann boundary conditions are prescribed. This leads to a simplification of A^{-}, with which the momentum equations at an outflow boundary are found. The boundary condition added is a prescription of pressure ($p = 0$). At inflow a fully developed inflow profile is prescribed; for example, for $x = \mathrm{const.}$ the equation solved is

$$\frac{\partial^2 u}{\partial y^2} + \frac{\partial^2 u}{\partial z^2} = G. \tag{16}$$

For the pressure, again a pressure equation is solved.

The resulting discretization is first-order-accurate and so-called positive. This discretization for a grid point for the 2D equations then looks like

$$\left[\begin{array}{ccc}
\begin{array}{c} -\frac{1}{Re}\Delta + 2u\partial_x + v\partial_y - \\ \frac{h}{2}\left(|v|\partial_{yy} + \frac{2u^2+c^2}{\sqrt{(u^2+c^2)}}\partial_{xx}\right) \end{array} &
\begin{array}{c} u\partial_y - \\ \frac{huv}{2(v^2+c^2)}[2\sqrt{(v^2+c^2)} - |v|]\partial_{yy} \end{array} &
\begin{array}{c} \partial_x - \\ \frac{hu}{2}\left(\frac{1}{\sqrt{(u^2+c_2)}}\partial_{xx} + \frac{\sqrt{(v^2+c^2)}-|v|}{v^2+c^2}\partial_{yy}\right) \end{array} \\
\begin{array}{c} v\partial_x - \\ \frac{huv}{2(u^2+c^2)}[2\sqrt{(u^2+c^2)} - |u|]\partial_{xx} \end{array} &
\begin{array}{c} -\frac{1}{Re}\Delta + u\partial_x + 2v\partial_y - \\ \frac{h}{2}\left(|u|\partial_{xx} + \frac{2v^2+c^2}{\sqrt{(v^2+c^2)}}\partial_{yy}\right) \end{array} &
\begin{array}{c} \partial_y - \\ \frac{hv}{2}\left(\frac{1}{\sqrt{(v^2+c^2)}}\partial_{yy} + \frac{\sqrt{(u^2+c^2)}-|u|}{u^2+c^2}\partial_{xx}\right) \end{array} \\
\begin{array}{c} c^2\partial_x - \\ \frac{hc^2u}{2\sqrt{(u^2+c^2)}}\partial_{xx} \end{array} &
\begin{array}{c} c^2\partial_y - \\ \frac{hc^2v}{2\sqrt{(v^2+c^2)}}\partial_{yy} \end{array} &
\frac{hc^2}{2}\left(\frac{1}{\sqrt{(u^2+c^2)}}\partial_{xx} + \frac{1}{\sqrt{(v^2+c^2)}}\partial_{yy}\right)
\end{array}\right], \tag{17}$$

where the three entries are for $(u, v, p)^{\mathrm{T}}$ respectively. Here ∂ represents a central discretization and the terms ∂_{xx} and ∂_{yy} are artificial dissipation terms.

In general it is favourable for iterative solution methods that from discretized equations so-called K-matrices[21] result. Irreducible K-matrices lead to M-matrices,[28] for which it is known that an efficient use of basic iterative methods is possible. However, often, as for the steady incompressible Navier–Stokes equations, a second-order discretization does not guarantee K-matrix properties, while the first-order upwind operator (e.g. with (9), (12) and (15)) does. With defect correction, second-order accuracy can be obtained by iterating with a first-order discretized operator. The right-hand side is then corrected with a second-order operator.

Suppose that N^1 is the operator resulting from first-order discretization and N^2 from second-order. Then iterative defect correction to solve $N^2(\mathbf{u}) = s$ looks like

```
find $\tilde{\mathbf{u}} = \mathbf{u}^{(0)}$
for $n = 1$ to $N$ do
    solve $N^1(\mathbf{u}^{(n)}) = s - N^2(\tilde{\mathbf{u}}) + N^1(\tilde{\mathbf{u}})$        (18)
    $\tilde{\mathbf{u}} = \mathbf{u}^{(n)}$
enddo.
```

It is shown in Reference 20 that defect correction converges to the second-order solution. The following equation has an interesting equivalence with (18):

$$\mathbf{u}^{(n)} = \mathbf{u}^{(n-1)} + \omega^n N^1(\mathbf{u}^{(n-1)})^{-1}[s - N^2(\mathbf{u}^{(n-1)})], \tag{19}$$

with $\omega^n = 1$. With adaptive choices of ω^n, additional acceleration could be obtained. This approach is not yet followed here.

Multigrid with defect correction is depicted in Figure 2. It starts with nested iteration on the coarsest grid (FMG) to find $\mathbf{u}^{(0)}$ in (18). After the finest grid has been reached, defect correction starts. Only on the finest grid is the right-hand side corrected. The second-order scheme used in defect correction is van Leer's κ-scheme.[19] The vectors $\mathbf{u}_{i,j,k}$ and $\mathbf{u}_{i+1,j,k}$ in (12), (13) or in (17) are replaced respectively by

$$\begin{aligned}
\mathbf{u}_{i,j,k} &\leftarrow \mathbf{u}_{i,j,k} + \frac{1+\kappa}{4}(\mathbf{u}_{i-1,j,k} - \mathbf{u}_{i,j,k}) + \frac{1-\kappa}{4}(\mathbf{u}_{i,j,k} - \mathbf{u}_{i+1,j,k}), \\
\mathbf{u}_{i+1,j,k} &\leftarrow \mathbf{u}_{i+1,j,k} + \frac{1+\kappa}{4}(\mathbf{u}_{i,j,k} - \mathbf{u}_{i+1,j,k}) + \frac{1-\kappa}{4}(\mathbf{u}_{i+1,j,k} - \mathbf{u}_{i+2,j,k}).
\end{aligned} \tag{20}$$

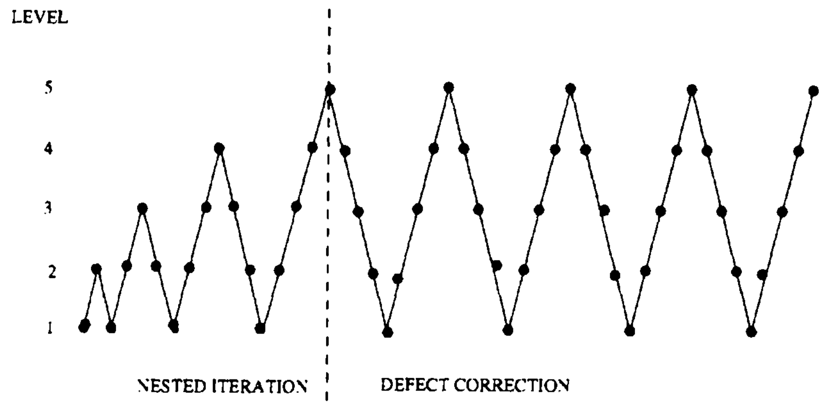

Figure 2. The defect correction strategy with five-level multigrid V-cycles and the start on the coarsest grid (nested iteration)

In the y- and z-direction the vectors $\mathbf{u}_{i,j,k}$, $\mathbf{u}_{i,j,k\pm1}$ and $\mathbf{u}_{i,j,k\pm1}$ are replaced in a similar way.

All tests have been done with $\kappa = 0$, the Fromm scheme. In Reference 17 for the steady compressible Navier–Stokes equations a limiter was needed to avoid wiggles near discontinuities. For the incompressible Navier–Stokes equations it is not necessary to implement a limiter. For many different problems at low and high Reynolds numbers, wiggles did not appear.

4. RESULTS

Solution algorithm

The parallel multigrid algorithm consists of a host and a node programme. The host programme takes care of the organization of input and output. It creates node processes, mails initial data to node processes and receives calculated results such as residuals from nodes. In the node programme the calculation takes place; also communication among nodes is taken care of. These communication tasks are taken care of by PARMACS-based[23] routines of the 3D communications library 'CLIC' (also used in Reference 29). With PARMACS-based routines, portability is guaranteed for a large class of parallel computers. Grid partitioning, the technique to distribute parts of a domain to different processes, is explained in many papers, for example in Reference 24. The domain is split into blocks. Along the arisen interior block boundaries an overlap region is placed. Therefore all operations in multigrid such as restriction, prolongation and relaxation can be performed in parallel. Keeping the values in overlap regions up to date on all multigrid levels requires communication among the nodes. It should be noticed that a first-order discretization requires an overlap region of one line of cells in order to achieve accuracy, while for the second-order discretization with (20) the stencil for evaluation of the right-hand side grows and a straightforward implementation of the parallel algorithm requires an overlap region of two cells. As smoother in the multigrid algorithm an alternating line Gauss–Seidel smoother is used, which updates every iteration on all lines of a block in two or three directions. Owing to the fact that curvilinear block-structured grids are employed, line smoothers can be used in general domains. This smoother is satisfactory for the problems considered. For driven cavity problems, one pre- and one post-smoothing iteration are used. For channel flow problems, two smoothings are performed at each visit. For all problems considered, it did not appear to be necessary to use underrelaxation factors in the smoother. The algorithm converged for all geometries and all Reynolds numbers considered, which is an interesting aspect.

Driven cavity flows

Already in Reference 16 the necessity for second-order-accurate solutions was shown; therefore we concentrate only on the defect correction solution method. In Reference 10, two benchmark problems are defined for 2D discretizations on non-orthogonal grids. The flow problems considered there are skewed driven cavity problems. The domain, depicted in Figure 3, is a parallelogram with boundary length $L = 1$. The angle β is 45° or 30°, so that highly non-orthogonal cells occur in the x-image of the grids. In this subsection our results will also be compared with the reference solutions and 3D equivalences will be introduced, for which the domain is also depicted in Figure 3. The top wall is moving with Cartesian velocity components $(u, v, w)^T = (1, 0, 0)^T$. On all other boundaries, $\mathbf{u} = 0$ is prescribed. The flow problems are also calculated in several other papers[5,30] for Reynolds numbers 100 and 1000.

We define three driven cavity test-cases: 1, the 2D square and 3D cubic driven cavity (angle $\beta = 90°$); 2, the skewed 2D and 3D cavity with angle $\beta = 45°$; 3, the skewed 2D and 3D cavity with angle $\beta = 30°$.

First the well-known 2D square driven cavity problem (test-case 1) is solved at $Re = 10^4$ in order to show that the discretization and defect correction technique lead to convergence for high Reynolds numbers. In Figure 4(a) the streamlines for this flow are presented. The recirculation zones are identical with those from Reference 31. In Figure 4(b) the centreline velocity components obtained along the lines cl1 (u-velocity) and cl2 (v-velocity) in Figure 3 for different grid sizes are presented and compared with the results from Reference 31. All results for this high Reynolds number compare very well. The sharp boundary layers near the walls are well captured. The four-block convergence factor found for the 513×513 grid for defect correction with the multigrid W(1,1)-cycle was 0·85.

For lower Reynolds numbers ($Re = 100$ and 1000) also very accurate 2D results were obtained, which are not shown here. The order of discretization accuracy for the flow at $Re = 10^4$ is checked with the help of the formula

$$\left|\frac{u_h - u_{2h}}{u_{2h} - u_{4h}}\right| = \left(\tfrac{1}{2}\right)^p, \qquad (21)$$

where u_h denotes the u-velocity on a grid of size h; the order of accuracy, p, is to be determined and is the interesting parameter. If the convergence of profiles is monotone, the parameter p in (21) gives a good indication of the order of accuracy by solving two problems on different grid sizes. Formula (21) is checked for this first test-case with the centreline velocities found at a point near a minimum: $y = 0·0625$. Table I presents these u-velocities found for the different grid sizes together with the value of p found from (21). It is found that the value of p on the finest grid is close to 2.

In several papers,[13,32,33] similar centreline velocity results are shown for the 3D cubic cavity. For $Re = 100$ and 1000 the centreline velocity profiles u along cl1 and w along cl2 are calculated as in References 13, 32 and 33. In Figure 5 these velocities are presented for our discretization. Solutions are

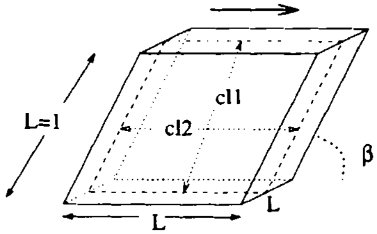

Figure 3. Domain for the two- and three-dimensional skewed driven cavity problem. The two-dimensional domain is the dashed mid-span plane

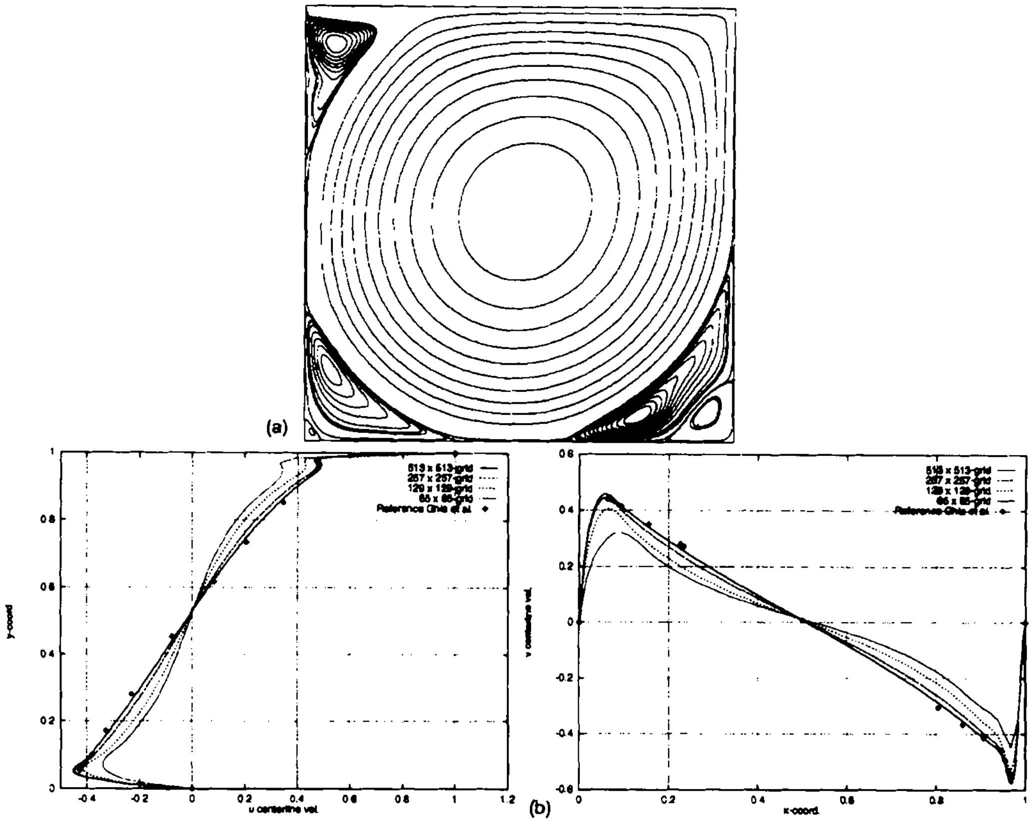

Figure 4. (a) Streamlines for flow at $Re = 10^4$ in a 2D driven cavity. (b) Centreline velocity components u along cl1 and v along cl2 for flow at $Re = 10^4$

presented on $17 \times 17 \times 17$, $33 \times 33 \times 33$ and $65 \times 65 \times 65$ grids and for $Re = 1000$ also on a $97 \times 97 \times 97$ grid which contains more than 900,000 grid points. For the fine grids the domain is split into eight blocks, each of which is solved on a processor of an MIMD computer, the IBM SP1 with 9 nodes. It is found that the convergence of the centreline velocities on all grid sizes for $Re = 100$ is very satisfactory. Already on the coarse grid with $17 \times 17 \times 17$ grid points the solution is qualitatively good. For $Re = 1000$ the solutions are quantitatively satisfactory from the $33 \times 33 \times 33$ grid. Clearly the centreline profiles are converging.

Table I. An investigation of the accuracy of the $Re = 10^4$ solution of the 2D square driven cavity problem

Grid	$u(y = 0{\cdot}0625)$	p
65×65	−0·33747	—
129×129	−0·41251	—
257×257	−0·43759	1·6
513×513	−0·44465	1·8

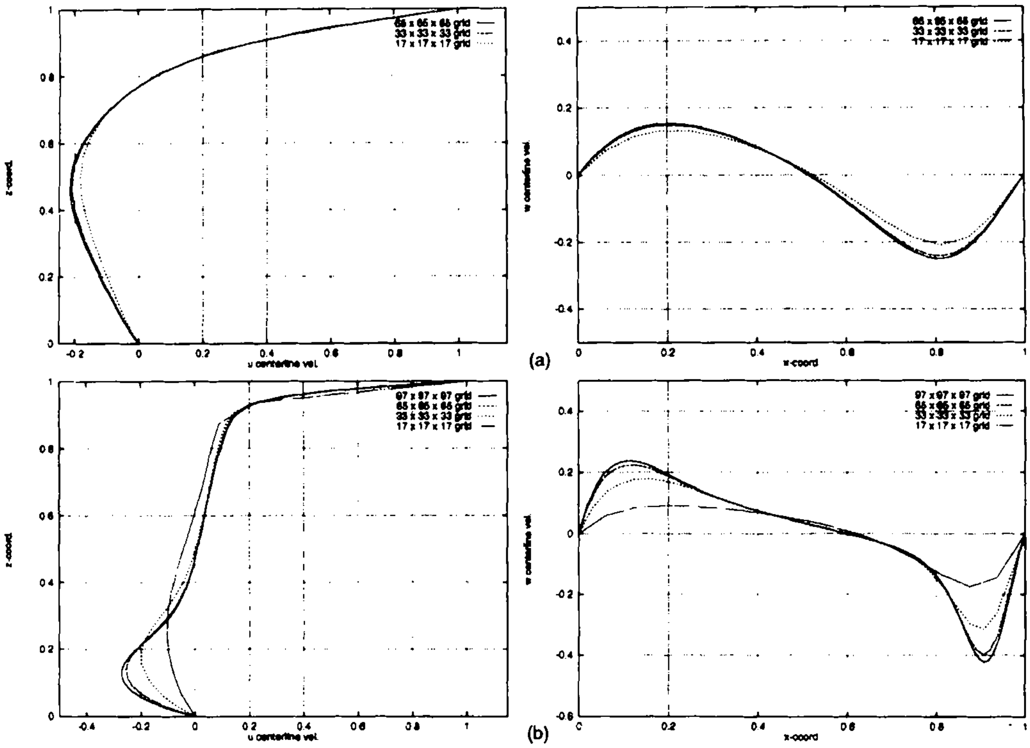

Figure 5. Centreline velocity components for flow at (a) $Re = 100$ and (b) $Re = 1000$ in a 3D cubic driven cavity for different grid sizes

Next, test-cases 2 and 3, the test-cases from Reference 10, are considered. The 2D discretization is investigated on four grids consisting of 33 × 33, 65 × 65, 129 × 129 and 257 × 257 cells. All streamline patterns for flows at $Re = 100$ and 1000 agree closely with those in Reference 10. The streamlines presented here in Figure 6 are for the flows at $Re = 1000$ for $\beta = 45°$ and 30°. Also the streamfunction values and positions compare very well with those in Reference 10.

The same is also true for the velocity profiles along the centrelines cl1 and cl2. Figure 7(a) shows the Cartesian velocity component u along the line cl1 for $Re = 100$, $\beta = 30°$; Figure 7(b) shows u along cl1 for $Re = 1000$, $\beta = 30°$. The behaviour of the velocity v along cl2 for this skewness angle as well as the behaviour of the velocity profiles for $\beta = 45°$ is similar and therefore not shown. It is remarkable that the centreline velocity profiles are already very satisfactory for relatively coarse grids (65 × 65). For a small number of unknowns, accurate results are obtained for both Reynolds numbers and both skewness angles.

These benchmark problems are generalized to 3D problems here. For $Re = 100$ and 1000 the centreline velocity profiles u along cl1 and w along cl2 are calculated on 17 × 17 × 17, 33 × 33 × 33 and 65 × 65 × 65 grids and for $Re = 1000$ also on 97 × 97 × 97 grid. The velocity profiles are shown in Figures 8 and 9 for both skewness angles. Again it is found that for $Re = 100$ all profiles are accurate, while for $Re = 1000$ the coarsest (17 × 17 × 17) grid appears to be too coarse to capture the features of the solution. A comparison among Figures 5, 8 and 9 shows that the discretization is as accurate in a rectangular cubic configuration as in skewed configurations; the convergence behaviour of the velocity profiles is identical. This is also a satisfactory conclusion.

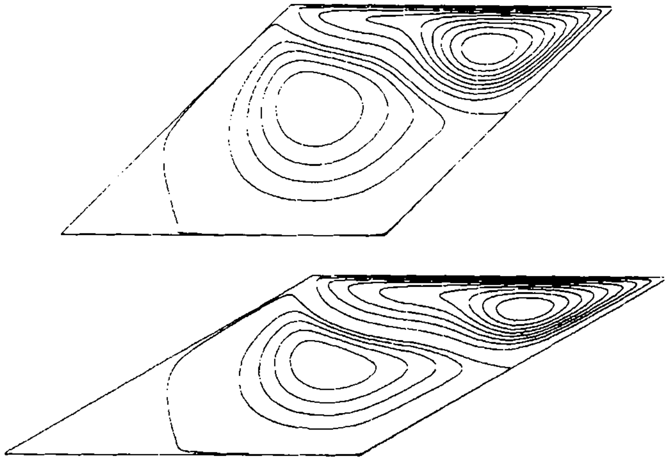

Figure 6. Streamlines for $Re = 1000$ for the 2D test-cases 2 and 3

Comparing Figures 7 and 9, it can be seen that for the 30° skewed cavity for $Re = 100$ the 2D and 3D results are alike. For $Re = 1000$ the results differ very much. The same conclusion is drawn in Reference 13 for the square and cubic cavity. Owing to these good results, the 3D discretization is also accurate. Finally, Figure 10 shows the eight-block multigrid convergence of the second-order residuals on the finest grid considered for the three test-cases for $Re = 100$ and 1000. For the flows at $Re = 100$ the multigrid V(1,1)-cycle is performed, for $Re = 1000$ the F(1,1)-cycle.

As can be seen in Figure 10, the second-order convergence is good for flows at $Re = 100$. For flows at $Re = 1000$ the convergence slows down, particularly for test-case 2 (a convergence factor of 0·86 is obtained) where the non-diagonal operator elements are very large. However, convergence was still observed, but further research to improve convergence for this test-case is needed. Convergence problems for steady calculations can also indicate an unsteady solution.

Three-dimensional flow in a 90° bending square duct

Next to non-orthogonality of grid cells, the curvature of grid lines is another important aspect for discretizations in curvilinear co-ordinates. This aspect is studied here by solving the 3D channel flow problem in a 90° bending square duct. Several researchers[1,12] have used the geometry presented in

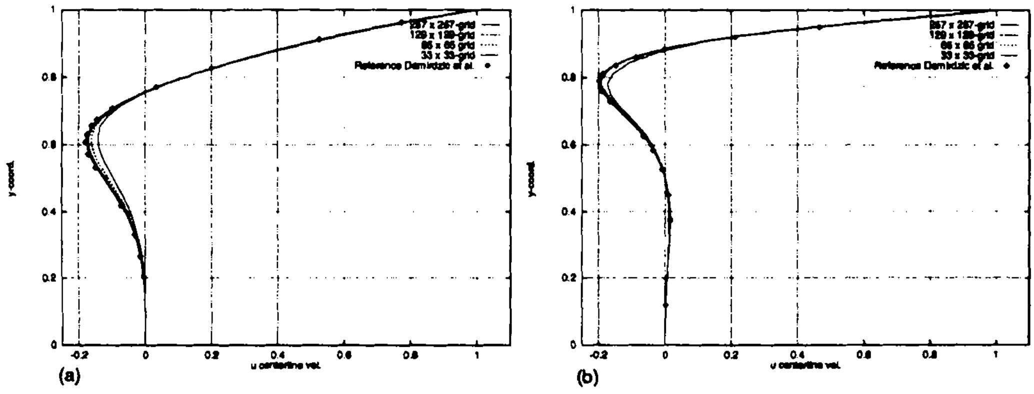

Figure 7. Two-dimensional skewed cavity u-velocity profiles along cl1 for $\beta = 30°$ and (a) $Re = 100$, (b) $RFe = 1000$

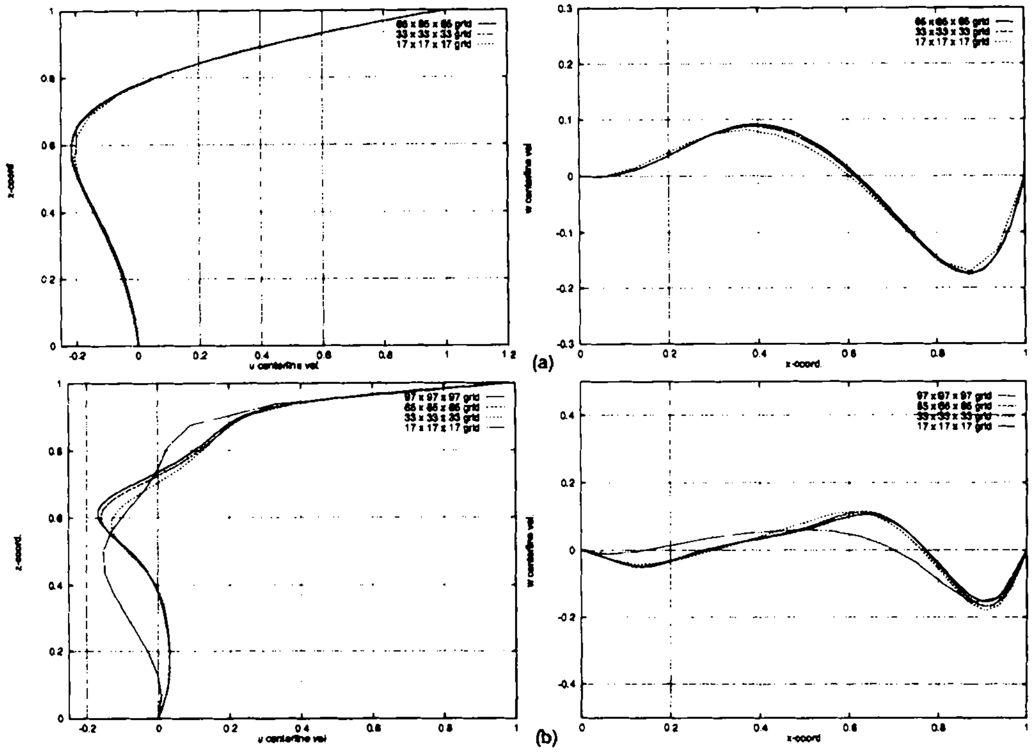

Figure 8. Three-dimensional centreline velocity components for flow at (a) $Re = 100$ and (b) $Re = 1000$ in a 3D skewed (angle $\beta = 45°$) driven cavity for different grid size

Figure 11, with $L = 5, h = 1$ and radius $R = 1{\cdot}8$ to test their discretizations for a flow at Reynolds number 790. For this Reynolds number also experimental results, namely streamwise velocities at several stations in the flow, are known.[34] The Reynolds number is based on the mean entrance velocity and the duct width. A fully developed inflow velocity profile from (16) is imposed at the inlet boundary. At the outflow boundary, Neumann boundary conditions are prescribed.

In References 1 and 12 the unsteady equations are solved with a fractional step method to the steady state solution. In Reference 1 a staggered non-uniform grid is used; in Reference 12 a collocated non-uniform grid is used. As mentioned before, we solve the steady equations directly with defect correction. The flow domain is split into three blocks as depicted in Figure 11. Two grids are investigated consisting of $73 \times 25 \times 17$ and $145 \times 49 \times 33$ grid points in length, width and height direction respectively. The grid points are uniformly distributed; each block consists of $25 \times 25 \times 17$ points for the first run and $49 \times 49 \times 33$ for the second. The symmetry of the problem is not taken into account here; symmetry conditions are not yet implemented.

In Figure 12(a) the streamwise velocities at six streamwise stations ($x = -5, -2{\cdot}5, 0; \theta = 30°, 60°, 90°$) for $z = 0{\cdot}5$ and $0{\cdot}25$ are presented as in References 1, 12 and 34. In Figure 12(b) the results presented in Reference 1 are also shown. Very satisfactory agreement is found at all six stations with other numerical reference results. The streamwise velocity peaks near the outside wall at stations 5 and 6 are very well captured. As in the other two references with numerical results, a difference from the experimental results can be observed at some of the stations.

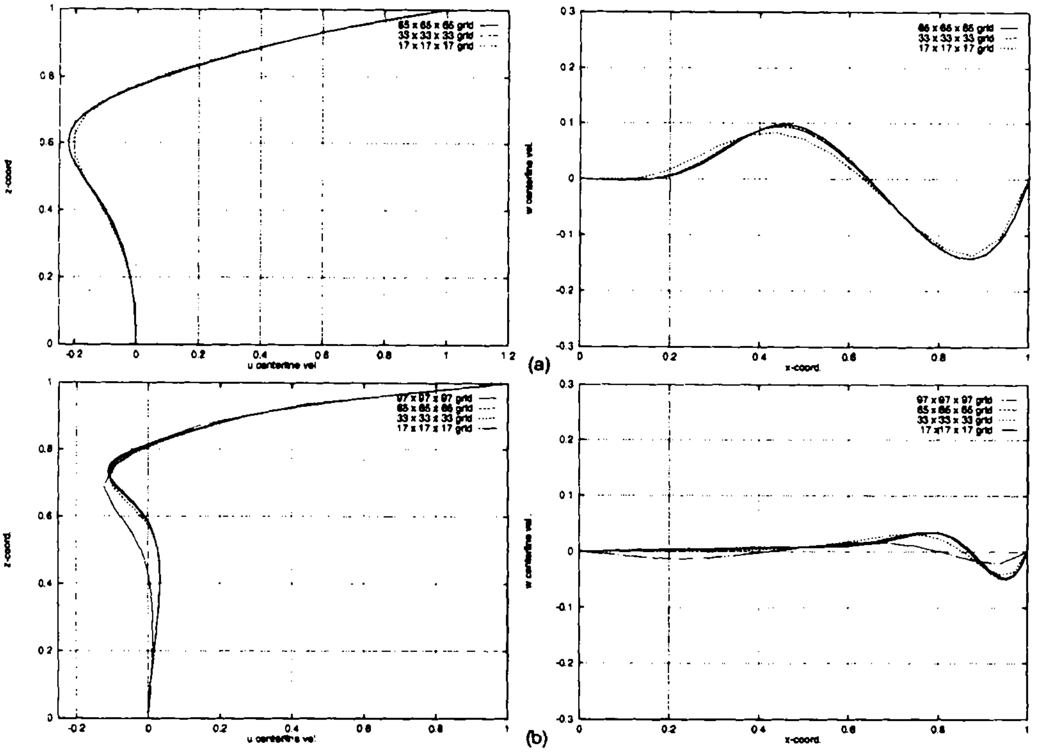

Figure 9. Three-dimensional centreline velocity components for flow at (a) $Re = 100$ and (b) $Re = 1000$ in a 3K skewed (angle $\beta = 30°$) driven cavity for different grid sizes

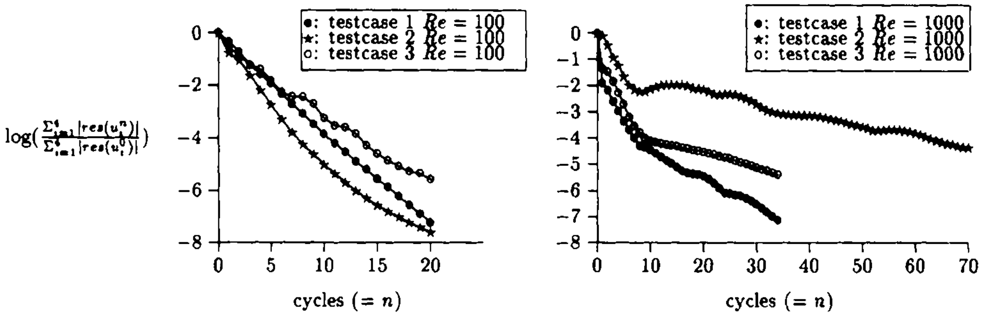

Figure 10. For the three-dimensional test-cases the eight-block convergence of second-order residuals with V(1,1)-cycles in defect correction for $Re = 100$ on a $65 \times 65 \times 65$ grid and F(1,1)-cycles for $Re = 1000$ on a $97 \times 97 \times 97$ grid

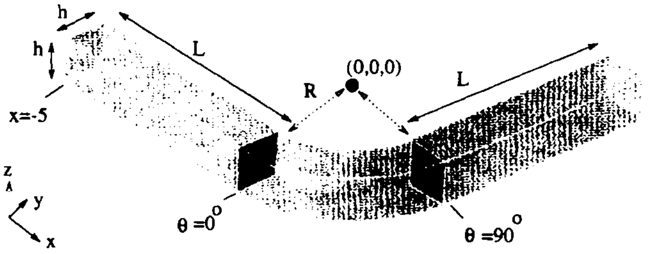

Figure 11. Domain for flow over a 3D square duct with a 90° bend and the division into three blocks

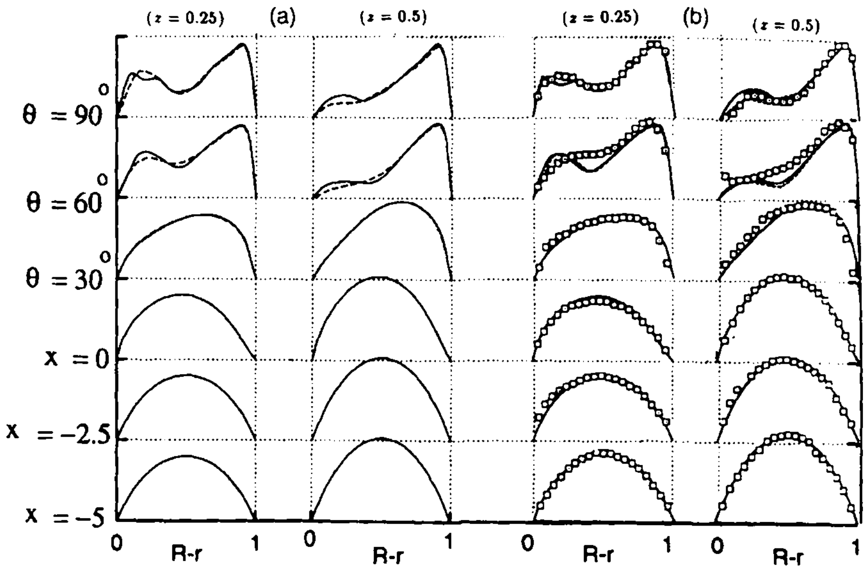

Figure 12. Comparison of streamwise velocity profiles at $z = 0{\cdot}25$ and $0{\cdot}5$ obtained on two different grids with reference results of Rosenfield *et al.*[1] (a) ———, Results on 145 × 49 × 33 grid; – – –, results on 73 × 25 × 17 grid. (b) ———, Results from Reference 1; – – –, results from Reference 1; □, experimental results from Reference 34

Now some other flow features will be presented, such as pressure contours at several cross-flow planes, obtained on a 73 × 25 × 25 grid in Figure 13(a). It can be seen that the main vortices are generated in the bend and diffuse in the downstream part. In Figure 13(b), two streamlines are depicted. One of the streamlines departs from the geometrical centre of the inflow part of the duct. It leaves the centreline and continues along the wall of the duct owing to the centrifugal force. The other streamline departs closer to the wall, $(x, y, z)^T = (-5, -2{\cdot}6, 0{\cdot}65)$. Its rotating path is seen clearly in Figure 13(b).

Furthermore, the cross-sectional velocity vector field at $\theta = 90°$ is plotted in Figure 14. The problem symmetry is clear; five different vorticities can be seen. The results on this coarse uniform grid compare satisfactorily with the results in Reference 12.

From the results presented above and the good agreement with the numerical reference results, it is concluded that the discretization can handle grids with strong curvature of grid lines. Finally, the multigrid convergence of the second-order results with F(2,2)-cycles is presented for both test runs in Figure 15.

Three-dimensional backward-facing flow

A well-known channel flow which is heavily studied for 2D discretizations (for example in References 35 and 36) is the laminar flow over a backward-facing step. For the 2D flow also experimental results are known.[37] Here 3D flow will be studied. The computations presented are for $Re = 200$, 400, 600 and 800, with the Reynolds number defined as

$$Re = \bar{U}(H - h)/\nu. \tag{22}$$

Here $\bar{U}$ is an average velocity defined as $\sqrt{[(1/N)\sum_i^N u^2]}$, with N the number of u-unknowns at the inlet boundary.

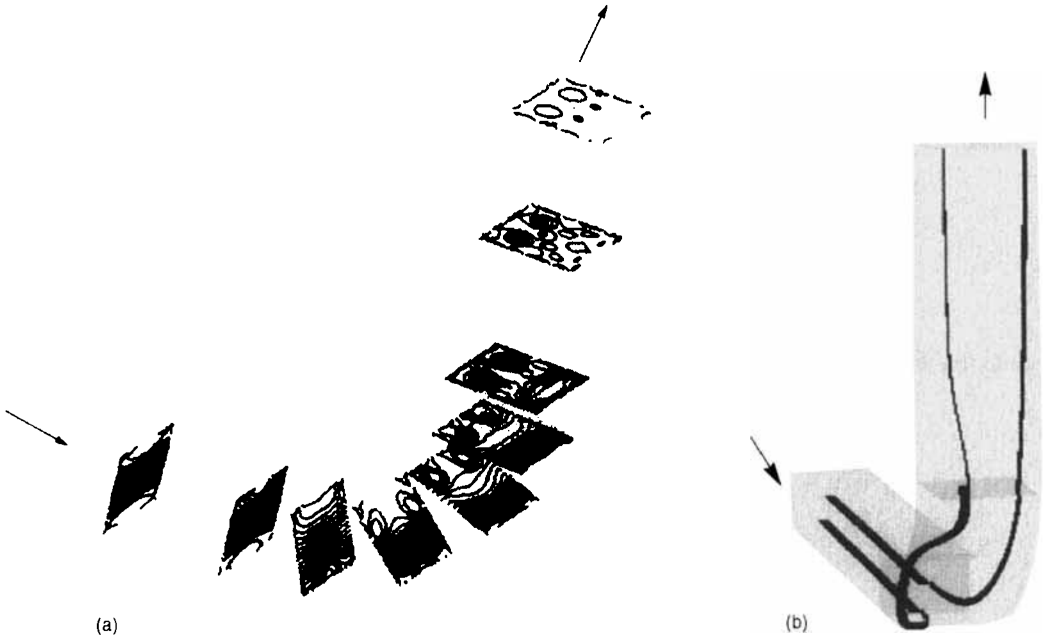

Figure 13. Features of the 3D flow in a 90° bending duct for $Re = 790$: (a) pressure contours in cross-sections; (b) two streamlines

Figure 16 shows the flow domain, which is split into nine blocks for parallel solution. The geometrical parameters are chosen as $L_1 = 50, L_2 = 10, H = 2, h_1 = 1$ and $h_2 = 1$for all Reynolds numbers. At the outflow boundary, Neumann boundary conditions are prescribed. At inflow a fully developed inflow is given, coming from (16).

The length of the recirculation zone (x_r) is determined for the Reynolds numbers investigated. It is defined as follows:

$$\text{if } (u_{i,j,k} < 0 \text{ and } u_{i+1,j,k} \geqslant 0), \quad \text{then } x_r = \tfrac{1}{2}(x_{i,j,k} + x_{i+1,j,k}), \quad \text{with } j \text{ such that } y_{i,j,k} = 0{\cdot}5. \tag{23}$$

This length is presented in Table II for two grid sizes containing $85 \times 17 \times 17$ and $165 \times 33 \times 33$ points.

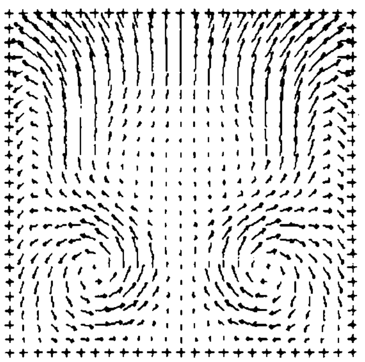

Figure 14. The velocity field in the cross-section at $\theta = 90^\circ$

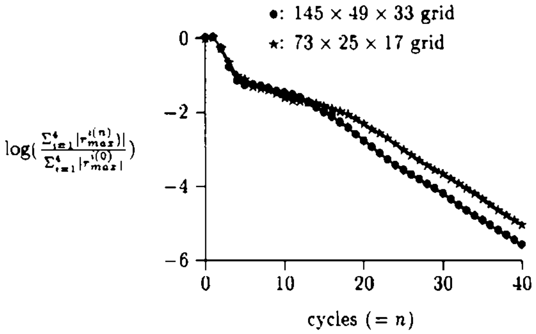

Figure 15. The three-block convergence of the second-order residuals with F(2,2)-cycles in defect correction for flow in a 90° bending duct on two grids, $Re = 790$

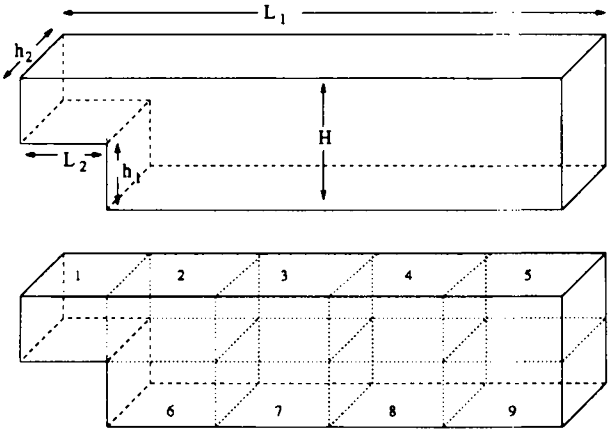

Figure 16. Domain for flow over a 3D backward-facing step and the division into nine blocks

Table II. The calculated length of the recirculation zone, x_r, in a 3D backward-facing step for for different Reynolds numbers

Reynolds number	x-value of reattachement point	
	Grid 85 × 17 × 17	Grid 165 × 33 × 33
200	4·69	4·53
400	8·44	8·28
600	12·19	12·34
800	16·56	16·09

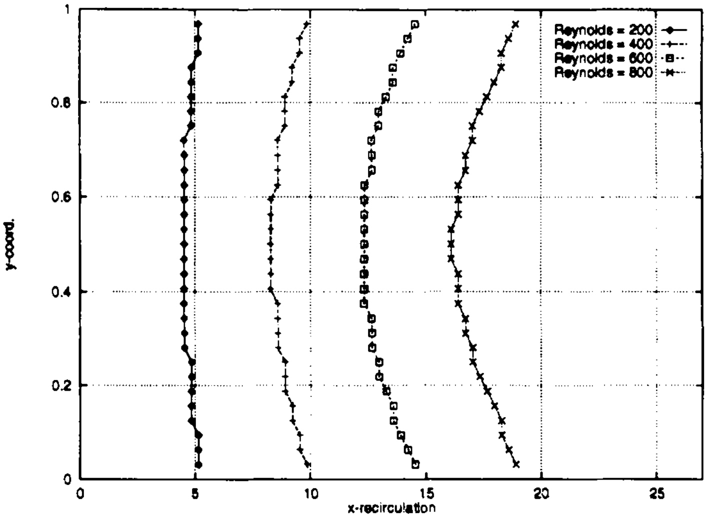

Figure 17. The shape of the recirculation length line along the y-axis for different Reynolds numbers

The recirculation lengths from Table II found for the two grids are already alike. The shape of the recirculation length line along the y-axis is shown in Figure 17. Here it can be seen that the lengths from Table II are actually minima; near the side wall boundaries of the domain the recirculation zones are largest. This shows the fact that the recirculation due to the step results in a truly 3D effect and that the flow is moving towards the channel centreline. For higher Reynolds numbers this effect is more pronounced.

In Figure 18, two selected streamlines showing the recirculation in the step and velocity vectors in the mid-span plane are shown for $Re = 400$. In Figure 19 these pictures are shown for $Re = 800$. In Figures 18 and 19 it can be observed that the streamlines that begin near a side wall enter the interior of the channel after the rotation near the step. This phenomenon is also shown in Reference 4 and, as mentioned before, influences the recirculation length. It is found that, contrary to the 2D results, a second recirculation zone near the upper wall of the channel did not appear with the geometry parameters chosen here. The nine-block multigrid defect correction convergence of the second-order residuals is shown in Figure 20. The multigrid cycle used is F(2,2). The convergence is satisfactory for all Reynolds numbers considered.

5. CONCLUSIONS

A 3D multiblock discretization for the steady incompressible Navier–Stokes equations in curvilinear coordinates is presented. The discretization is based on a flux difference formulation of the equations. A collocated grid arrangement of primitive variables, Cartesian velocity unknowns and pressure is used. The 3D algorithm is based on an existing 2D code which is first investigated for some driven cavity benchmark problems. The 2D benchmark solutions show that our code is a reliable solver for the 2D incompressible Navier–Stokes equations on non-orthogonal grids. For Reynolds numbers 100 and 1000, very accurate results are obtained with a small number of grid points.

Also for 3D problems the code produces satisfactory results. The centreline velocity profiles obtained in a cubic cavity compare very well with results from other papers. The convergence behaviour of velocity profiles in skewed 3D cavities with highly non-orthogonal grid cells is similar to the behaviour of the profiles in a cubic cavity with rectangular cells. Next to the non-orthogonality of grid cells, it is

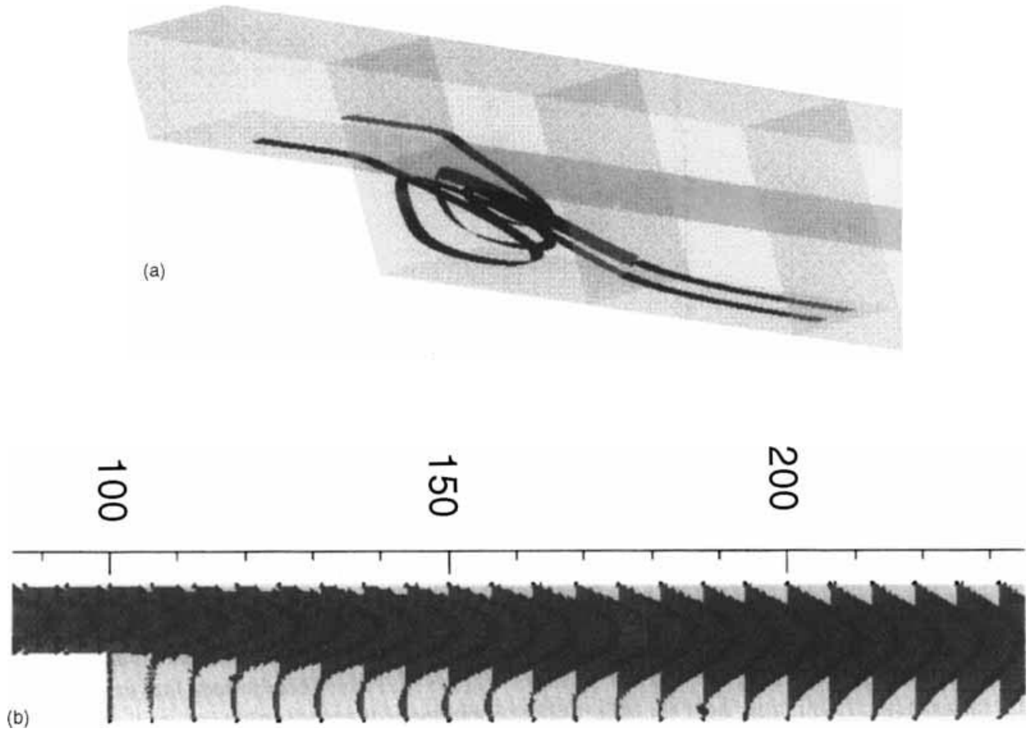

Figure 18. Three-dimensional flows over a backward-facing step (different blocks, all 17 x 17 x 17, are also visible in (a)) at $Re = 400$: (a) two selected streamlines showing the recirculation; (b) velocity vectors in the mid-span plane

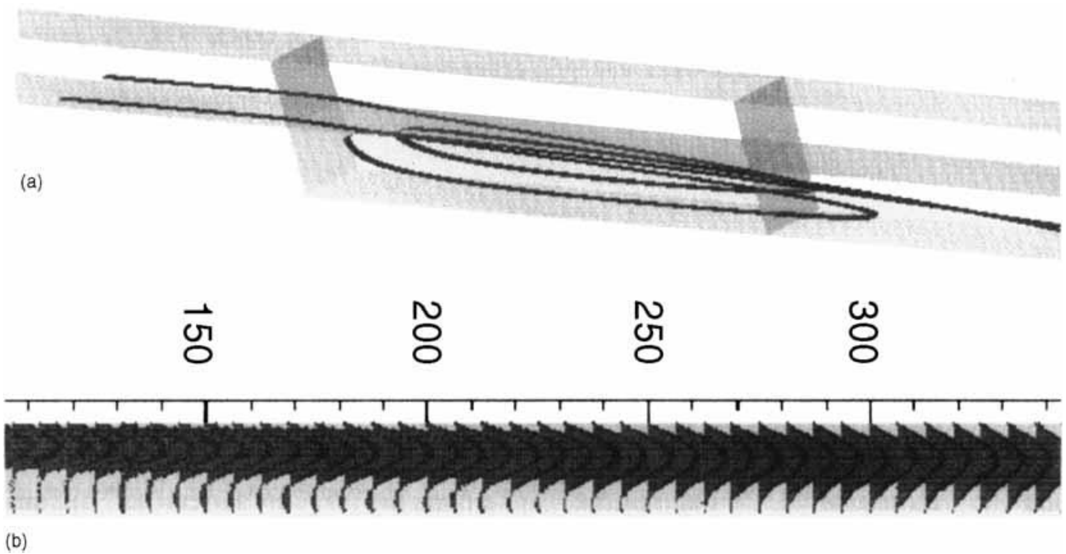

Figure 19. Three-dimensional flow over a backward-facing step (different blocks, all 17 x 17 x 17, are also visible in (a)) at $Re = 800$: (a) two selected streamlines showing the recirculation; (b) velocity vectors in the mid-span plane

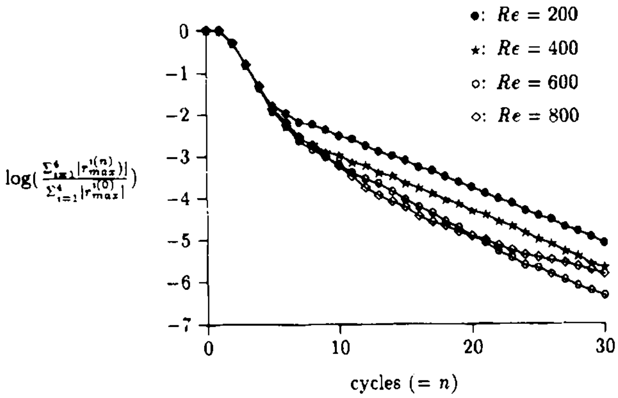

Figure 20. The nin-block convergence of the second-order residuals with F(2,2)-cycles in defect correction for backward-facing step flow on the finest grid comprising 165 × 33 × 33 points

found that the discretization can handle strong grid curvature very well. Very satisfactory agreement is found between the numerical results obtained and reference results from other papers for the flow in a 90° bending duct. Also the flow in a 3D backward-facing step is investigated, for which recirculation lengths are presented.

It is found that the multigrid algorithm with the defect correction technique is a reliable solver for the problems investigated. It did not appear to be necessary to use underrelaxation factors in the alternating line Gauss–Seidel smoother for convergence. The multiblock algorithm converges very well for the driven cavity problems at Reynolds number 100. The results for channel problems were also satisfactory. The convergence for skewed driven cavity problems at Reynolds number 1000 needs improvement and further investigation.

ACKNOWLEDGEMENTS

Dr. A. Schüller, Dr. B. Steckel and Dr. J. Wu are gratefully acknowledged for fruitful discussions and for the line smoother, and G. Umlauf for providing his REDUCE environment.

REFERENCES

1. M. Rosenfeld, D. Kwak and M. Vinokur, 'A fractional step solution method for the unsteady incompressible Navier–Stokes equations in generalized coordinate systems', *J. Comput. Phys.*, **94**, 102–137 (1991).
2. M. Rosenfeld and D. Kwak, 'Multigrid acceleration of a fractional step solver in generalized coordinate systems', *AIAA Paper 92-0185*, 1992.
3. A. Segal, P. Wesseling, J. van Kan, C. W. Oosterlee and C. G. M. Kassels, 'Invariant discretization of the incompressible Navier–Stokes equations in boundary fitted co-ordinates', *Int. j. numer. methods fluids*, **15**, 411–426 (1992).
4. S. Zeng and P. Wesseling, 'Multigrid solution of the incompressible Navier–Stokes equations in general coordinates', *SIAM J. Numer. Anal.*, **31**, 1764–1784 (1994).
5. P. He and M. Salcudean, 'A numerical method for 3D viscous incompressible flows using non-orthogonal grids', *Int. j. numer. methods fluids*, **18**, 449–468 (1994).
6. T. Ikohagi and B. R. Shin, 'Finite difference schemes for steady incompressible Navier–Stokes equations in general curvilinear coordinates', *Comput. Fluids*, **19**, 479–488 (1991).
7. T. Ikohagi, B. R. Shin and H. Daiguji, 'Application of an implicit time-marching scheme to a three-dimensional incompressible flow problem in curvilinear coordinate systems,' *Comput. Fluids*, **21**, 163–175 (1992).
8. C. M. Rhie and W. L. Chow, 'A numerical study of the turbulent flow past an isolated airfoil with trailing-edge separation', *AIAA J.*, **21**, 1525–1532 (1983).
9. M. Peric, 'A finite volume method for the three-dimensional fluid flow in complex ducts', *Ph.D. Thesis*, University of London, 1985.

10. I. Demirdzic, Z. Lilek and M. Peric, 'Fluid flow and heat transfer test problems for non-orthogonal grids: bench-mark solutions', *Int. j. numer. methods fluids*, **15**, 329–354 (1992).
11. K. M. Smith, W. K. Cope and S. P. Vanka, 'A multigrid procedure for three dimensional flows on non-orthogonal colocated grids', *Int. j. numer. methods fluids*, **17**, 887–904 (1993).
12. Y. Zang, R. L. Street and J. R. Koseff, 'A non-staggered grid, fractional step method for time-dependent incompressible Navier–Stokes equations in curvilinear coordinates', *J. Comput. Phys.*, **114**, 18–33 (1994).
13. V. Babu and S. A. Korpela, 'Numerical solution of the incompressible Navier–Stokes equations', *Comput. Fluids*, **23**, 675–691 (1994).
14. D. Kwak, J. L. C. Chang, S. P. Shanks and S. R. Chakravarthy, 'A three dimensional incompressible Navier–Stokes flow solver using primitive variables,' *AIAA J.*, **24**, 390–396 (1986).
15. S. E. Rogers and D. Kwak, 'Upwind differencing scheme for the time-accurate incompressible Navier–Stokes equations', *AIAA J.*, **28**, 253–262 (1990).
16. E. Dick and J. Linden, 'A multigrid method for steady incompressible Navier–Stokes equations based on flux difference splitting', *Int. j. numer methods fluids*, **14**, 1311–1323 (1992).
17. B. Koren, 'Defect correction and multigrid for an efficient and accurate computation of airfoil flows', *J. Comput. Phys.*, **77**, 183–296 (1988).
18. E. Dick, 'Multigrid methods for steady Euler and Navier–Stokes equations based on polynomial flux-difference splitting', in W. Hackbusch and U. Trottenberg (eds), *Multigrid Methods III*, Birkhäuser, Basel, 1991, pp. 277–288.
19. B. van Leer, 'Upwind-difference methods for aerodynamic problems governed by the Euler equations', in B. Enquist, S. Osher and R. Somerville (eds), *Large Scale Computations in Fluid Mechanics*, Vol. 22, II, American Mathematical Society, Providence, RI, 1985, pp. 327–336.
20. W. Hackbusch, *Multi-grid Methods and Applications*, Springer, Berlin, 1985, p. 288.
21. P. Wesseling, *An Introduction to Multigrid Methods*, Wiley, Chichester, 1992.
22. H. Ritzdorf, A. Schüller, B. Steckel and K. Stüben, '$L_i SS$—an environment for the parallel multigrid solution of partial differential equations on general domains', *Parallel Comput.*, **20**, 1559–1570 (1994).
23. R. Calkin, R. Hempel, H. C. Hoppe and P. Wypior, 'Portable programming with the PARMACS message-passing library', *Parallel Comput.*, **20**, 615–632 (1994).
24. J. Linden, B. Steckel and K. Stüben, 'Parallel multigrid solution of the Navier–Stokes equations on general 2D-domains', *Parallel Comput.*, **7**, 461–475 (1988).
25. A. C. Hearn, *REDUCE User's Manual Version 3.5*, *RAND Pub. CP78*, RAND, Santa Monica, CA, 1993.
26. M. Vinokur, 'An analysis of finite-difference and finite-volume formulations of conservation laws', *J. Comput. Phys.*, **81**, 1–52 (1989).
27. R. Peyret and T. D. Taylor, *Computational Methods for Fluid Flow*, Springer, Berlin 1983, p. 108.
28. R. S. Varga, *Matrix Iterative Analysis, Prentice-Hall, Englewood Cliffs, NJ, 1962.*
29. B. Eisfeld, H.-M. Bleecke, N. Kroll and H. Ritzdorf, 'Structured grid solvers II, Parallelization of block structured flow solvers', in *Parallel Computing in Computational Fluid Dynamics*, Von Karman Institute, Rhode Saint Genèse, 1–20 1995.
30. C. W. Oosterlee, P. Wesseling, A. Segal and E. Brakkee, 'Benchmark solutions for the incompressible Navier–Stokes equations in general coordinates on staggered grids', *Int. j. numer. methods fluids*, **17**, 301–321 (1993).
31. U. Ghia, K. N. Ghia and C. T. Shin, 'High-Re solutions for incompressible flow using the Navier–Stokes equations and a multigrid method', *J. Comput. Phys.*, **48**, 387–411 (1982).
32. A. B. Cortes and J. D. Miller, 'Solution of the Navier–Stokes equations by the spectral-difference method', *Numer. Methods Partial Diff. Eq.*, **10**, 345–368 (1994).
33. H. C. Ku, R. S. Hirsh and T. D. Taylor, 'A pseudospectral method for solution of the three-dimensional incompressible Navier-Stokes equations,' *J. Comput. Phys.*, **70**, 439–462 (1987).
34. J. A. C. Humphrey, A. M. K. Taylor and J. H. Whitelaw, 'Laminar flow in a square duct of strong curvature', *J. Fluid Mech.*, **83**, 509–527 (1977).
35. J. Kim and P. Moin, 'Application of a fractional-step method to incompressible Navier–Stokes equations', *J. Comput. Phys.*, **59**, 308–323 (1985).
36. M. C. Thompson and J. H. Ferziger, 'An adaptive multigrid technique for the incompressible Navier–Stokes equations', *J. Comput. Phys.*, **82**, 94–121 (1989).
37. B. F. Armaly, F. Durst, J. C. F. Pereira and B. Schönung, 'Experimental and theoretical investigation of backward-facing step flow', *J. Fluid Mech.*, **127**, 473–496 (1983).